Effect of polymers on the nanostructure and on the carbonation of calcium silicate hydrates: a scanning transmission X-ray microscopy study

J. Ha · S. Chae · K. W. Chou · T. Tyliszczak ·
P. J. M. Monteiro

Abstract This study investigated the effects of organic polymers (polyethylene glycol and hexadecyltrimethylammonium) on structures of calcium silicate hydrates (C–S–H) which is the major product of Portland cement hydration. Increased surface areas and expansion of layers were observed for all organic polymer modified C–S–H. The results from attenuated total reflectance–Fourier transform infrared (ATR–FTIR) spectroscopic measurements also suggest lowered water contents in the layered structures for the C–S–H samples that are modified by organic polymers. Scanning transmission X-ray microscopy (STXM) results further supports this observation. We also observed difference in the extent of C–S–H carbonation due to the presence of organic polymers. No calcite formed in the presence of HDTMA whereas formation of calcite was observed with C–S–H sample modified with PEG. We suggest that the difference in the carbonation reaction is possibly due to the ease of penetration and diffusion of the CO_2. This observation suggests that CO_2 reaction strongly depends on the presence of organic polymers and the types of organic polymers incorporated within the C–S–H structure. This is the first comprehensive study using STXM to quantitatively characterize the level of heterogeneity in cementitious materials at high spatial and spectral resolutions. The results from BET, XRD, ATR–FTIR, and STXM measurements are consistent and suggest that C–S–H layer structures are significantly modified due to the presence of organic polymers, and that the chemical composition and structural differences among the organic polymers determine the extent of the changes in the C–S–H nanostructures as well as the extent of carbonation reaction.

Introduction

Calcium silicate hydrate (C–S–H) is the primary binding phase in Portland cement concrete and forms a poorly crystallized or nanostructure with various compositions. Results from a number of previous studies indicate that C–S–H has a layer structure and forms a rigid gel with a pore solution [1–3]. Performance of cement-based materials are essentially determined by this pore structure and composition of solid phase, hence the nanostructure of C–S–H essentially governs and impacts the overall property of the cementitious materials [4–6]. Therefore, changes in the nanostructure of C–S–H can have a significant effect on concrete performance. In past, C–S–H(I) has been noted as the more crystalline phase in C–S–H that are found in the hydrated Portland cement paste. In many structural models, C–S–H(I) has been regarded as an imperfect form of tobermorite and used to study the structural changes of C–S–H at molecular-level. In this study, we have synthesized C–S–H in the laboratory and hereon noted as C–S–H to distinguish from the C–S–H(I) of the alkali-activated slag cement.

In this study, we also synthesize composites that are composed of polymer modified C–S–H and investigate how the structural variation of the polymers influence the intercalation of polymers into the C–S–H structure.

Several studies have shown that mechanical properties of cement-based materials are enhanced upon the modification of C–S–H structure with polymers through ionic

J. Ha (✉) · S. Chae · P. J. M. Monteiro
Department of Civil and Environmental Engineering,
University of California-Berkeley, Berkeley, CA 94720, USA
e-mail: juyoung@berkeley.edu

K. W. Chou · T. Tyliszczak
Advanced Light Source, Lawrence Berkeley National
Laboratory, Berkeley, CA 94720, USA

bonding and/or adsorption reaction at defect sites [7–10]. For example, Minet et al. [11] showed an increase of the basal distance of C–S–H(I) with the content of trialkoxysilane, suggesting the incorporation of organic moieties in the interlayer. They concluded that the inorganic framework of C–S–H(I) was not disrupted due to the organic polymers based on their ^{29}Si NMR data. On the contrary, Merlin et al. [12] indicated no specific intercalation of macromolecules into C–S–H(I) layer structure. They suggested that the composite materials do not form via incorporation of macromolecules into the layers but through crystallization of aggregates because the steric and entropic factor can prevent macromolecules entering into C–S–H(I) layer structures. As these previous studies indicate, the interaction of polymeric substances with C–S–H is still controversial and more detailed understanding and careful study must be preformed before generalizing the nature of polymer interaction with C–S–H.

Furthermore, the reaction mechanisms of organic polymer modified C–S–H are expected to be different from the one of unmodified C–S–H. One of the most important reactions is carbonation of concrete and it is a complex physicochemical process that slowly changes and modifies the structure of concrete. In this study, we have also investigated the difference in the carbonation reaction mechanisms of C–S–H due to the modification by organic polymers.

In the past, the highly heterogeneous cementitious materials have been analyzed by a variety of analytical techniques such as X-ray diffraction (XRD), transmission electron microscopy (TEM), nuclear magnetic resonance (NMR), and scanning electron microscopy (SEM) [13–15]. Recent studies have utilized electron energy loss spectroscopy (EELS) and Fourier transformed infrared (FTIR) spectroscopy [16–19]. These studies have demonstrated that chemical speciation of elements in heterogeneous materials on the micro-scale. However, the above listed analytical approaches have certain limitations. Recently, synchrotron-based X-ray absorption spectroscopy (XAS) has been used to study cement paste [17–19]. The main advantage of using synchrotron based X-ray source is the high photon flux, high brilliance, and high wavelength tuneability with focused beams.

Although bulk XAS provides speciation of chemical entities in complex matrixes can be determined at ppm levels, often it does not provide spatial information. Instead of bulk-XAS, it is important to have analytical tool observing both spectroscopic and spatial information down to nano- to micrometer scale because the cementitious materials exhibit sub-micron structural heterogeneities and such information may reveal that different chemical environments within C–S–H. In this project, we have used scanning transmission X-ray microscopy (STXM) to resolve both the spatial resolution and speciation limitation problems with the current experimental methods [20–22].

STXM is a transmission microscopy using a monochromated X-ray beam produced by synchrotron radiation. X-ray absorption edges occur when an incident photon energy exceeds the binding energy needed to remove completely, i.e., ionize, an electron from an orbital shell. For example, photons with energy just below the ionization edge of carbon (280–300 eV in the case of carbon 1 s electron) can promote core electrons into a variety of bound states that correspond to unoccupied or partially occupied molecular orbitals. As a result, different near edge absorption bands are observed and these bands are sensitive indicators of the local chemical bonding environment surrounding the atom of interest. In addition to obtaining the chemical speciation information, STXM allows identifying heterogeneity within the samples on a particle-by-particle basis. Using the scanning transmission X-ray microscopy (STXM) together with concurrent measurements of near-edge X-ray absorption fine structure (NEXAFS) spectra, it is possible to examine sample compositions and spatial heterogeneities.

To study the effects of different polymers on nanostructure of C–S–H, two different types of modified C–S–H were studied; polyethylene glycol (PEG) modified C–S–H and hexadecyltrimethylammonium (HDTMA) modified C–S–H. Furthermore, we have exposed the organic modified C–S–H samples for carbonation reaction. Using STXM in combination with other conventional experimental approaches, results from this study will improve understanding of role of polymers on nanostructure and carbonation reaction of C–S–H, bringing the state of art a step closer to a development of modified cement pastes.
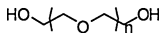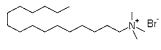
Experimental

Materials and sample preparation

C–S–H samples, hereon noted as CSH, with C/S ratio of 1.6 were prepared using stoichiometric amounts of CaO and amorphous silica mixed at a water-solids ratio of about 11.8. The CaO was produced using precipitated $CaCO_3$ heated at 900 °C for 1 day. The CaO was stored under N_2 environment until mixed with amorphous silica purchased from Cabosil. The mixed reactants resulting CSH was continuously mixed for 1 year at 23 °C. The final materials were filtered and dried under vacuum for 4 days and stored under N_2 environment.

HDTMA modified C–S–H samples, hereon noted as HDTMA–CSH, were prepared by reacting the prepared C–S–H with excess aqueous 0.01 M HDTMA-Br for 24 h followed by washing with deionized (DI) water until Br

Table 1 Molecular structure and weight of the polymers used to modify CSH

Chemical name	Chemical formula	Molecular weight (g/mol)	Structure
Polyethylene glycol (PEG)	$H(OCH_2CH_2)_nOH$	200	
Hexadecyltrimethylammonium, bromide (HDTMA)	$C_{19}H_{42}BrN$	354.46	

was not detected with $AgNO_3$. All mixing was done under N_2 environment. Samples are vacuum-dried for 12 h until further use.

PEG200 modified C–S–H samples (i.e., PEG200 stands for polyethylene glycol of molecular weight of 200), hereon noted as PEG200-CSH, was prepared by mixing the CSH with the heated PEG200 at 65–70 °C for 24 h. All mixing was done under N_2 environment. At the end of the reaction run, the final product was filtered and washed with methanol to remove the excess polymer.

All chemical reagents used in sample preparation are purchased from Fisher Scientific. Table 1 shows the molecular structure and information of the polymers used in this study. For carbonated C–S–H samples, the organic modified C–S–H samples are exposed to CO_2 for 2 days with CO_2 bubbled through the samples that are submerged in deionized Milli-Q water at a flow rate of 3 mL/h to accelerate carbonation.

Sample characterization

Powder XRD patterns have been analyzed by a standard procedure. Crystalline phases were identified. Samples were analyzed by XRD from a 2θ value of 5–55° with a Rigaku Rotaflex RU200B instrument using a step of 0.02° and Cu Kα_1 radiation at 30 kV, 15 mV.

The Brunauer–Emmett–Teller (BET) surface area measurement (i.e., room temperature N_2 adsorption–desorption analysis) was measured using ASAP 2000 Micrometrics instrument. For BET measurements, samples were first dried under vacuum at room temperature for 3 days. A five-point BET analysis was performed for each sample.

Attenuated total reflectance–Fourier transform infrared (ATR–FTIR) spectroscopic measurements of polymer modified CSH samples were performed using Nicolet FT–IR spectrometer (NEXUS470), equipped with a mercury cadmium telluride (MCT) detector and a horizontal attenuated total reflectance attachment (germanium crystal). Data collection and spectral calculations were done using OMNIC software (version 6.0a, Nicolet Instrument Corp.). Wet paste samples for ATR–FTIR analysis were prepared by separating and concentrating the samples by centrifugation of each sample at $10,000 \times g$ for 15 min. The supernatant was decanted and a thin layer of the concentrated wet paste of each sample was uniformly applied directly to the germanium (Ge) ATR crystal with a small volume of the decanted supernatant being applied on top of wet paste layer to prevent drying of the samples. The sample holding region was sealed with a lid to prevent evaporation during ATR–FTIR measurements. 500 scans were collected and averaged per sample with a spectral resolution of 4 cm^{-1}. The strong spectral contribution of water was removed from the ATR–FTIR spectrum of each sample spectrum by subtracting the spectrum of a supernatant solution. The normalization and baseline correction of ATR–FTIR spectra were done with great care so as not to enhance or diminish the magnitude of any spectral peaks or to shift the peak positions.

STXM (Scanning transmission X-ray microscopy) analysis

Two different types of results were collected at the STXM beamline. First, an image contrast data is obtained from differential absorption of X-rays depending on the chemical composition of the sample. Second, image stacks or line scan data are obtained by scanning the sample in the x–y direction (image stack) or x direction (line scan) of selected sample areas at energy increments of 0.1 eV over the energy range of interest (e.g., 280–305 eV for carbon, 342–360 eV for calcium, 1825–1890 eV for silica). Here, x refers to the horizontal direction, y to the vertical direction, and the x–y plane to the plane perpendicular to the X-ray beam. In addition to 2-dimensional images, the stack image produces NEXAFS spectrum for a specific element on each pixel of the image.

As noted in the introduction section, in STXM, the soft X-ray beam is generated by a synchrotron light source and beamline, and focused to a small point by a Fresnel zone plate. The transmitted X-rays are detected and the obtained transmission images are collected by a scan of the sample. The chemical information of the sample is obtained in point, line or image mode by acquiring signal at multiple photon energies. Hence, the primary signal measured in STXM is transmitted intensity as a function of energy

(i.e., collected as spectra) or position (i.e., collected as images). In data analysis procedure, this signal collected in STXM is converted to optical density (OD) which is sensitive to sample thickness, density, and composition. The following equation illustrates the relationship among the OD, density, and sample properties:

$$OD = -\ln(I/I_0) = \sigma \cdot t = \mu \cdot \rho \cdot t$$

where σ is the linear absorption coefficient, t is the sample thickness, and μ is the mass absorption coefficient, and ρ is the density of the sample. Hence, measuring the set of pixels and converting the data to OD with the incident flux generates an X-ray OD image at a single photon energy. Changing the photon energy and taking images with other photon energies generate an image sequence, or called stack, which includes chemical information as well as topographical information.

One pixel can be as small as 25–30 nm. Counting times for the images are in the order of few milliseconds or less per pixel. Energy calibration was accomplished using the well-resolved 3p Rydberg peak of gaseous CO_2 for the C K-edge, quartz for Si K-edge, and calcite for Ca $L_{II,III}$-edge. Normalization and background subtraction of the spectra were performed by dividing each spectrum from the sample by the spectrum of the sample-free location. Elemental maps of the samples can be obtained by subtracting the image obtained from the below the absorption energy level and the image obtained above the absorption energy. Axis 2000 software (version 2.1) [23] was used to align image stacks and extract NEXAFS spectra from image stack or line scan measurements. In this study, the STXM results were collected at the Advanced Light Source (ALS) branch line 11.0.2.2 and 5.3.2 with the synchrotron storage ring operating at 1.9 GeV and 200–400 mA stored current. Counting times are of the order of a few milliseconds or less per pixel to avoid beam damage.

ALS branch line 11.0.2.2 and 5.3.2 use 30 nm zone plate and these branch lines are designated for environmental and chemical studies. At STXM beam station 11.0.2.2 at ALS, which is capable of 25–30 nm spatial resolution over the energy range 75–2150 eV for imaging and obtaining NEXAFS spectrum, we are the first research group conducting a comprehensive study on C–S–H using this novel, state-of-art technique to quantitatively characterize the level of heterogeneity in cementitious materials at the high spatial and spectral resolutions over a broad energy range from carbon to silica. Samples were prepared by suspending 10 mg of dried samples in 500 μL of DI MilliQ water. Approximately 10 μL of the suspended samples were taken and placed on silicon nitride membrane window. All sample preparations were done under N_2 conditions until loaded to STXM experimental chamber. The experimental chambers are quickly vacuumed and prepared for the measurements. Each sample was focused each time the energy of interest was changed. After focusing, image contrast measurements were performed to identify the elemental locations and line scans were performed on the interested location to further obtain the NEXAFS spectrum. Once it was confirmed that the specific sample area contains interesting spectral information, image stack was performed. Beam damage on samples was occasionally checked by measuring the NEXAFS spectra before and after the long image stack. At least three different measurements on different sampling positions were taken per each sample in order to increase the reliance of the data.

Results and discussions

BET and XRD results

Surface area of cement paste mostly originates from the formation of the porous phase C–S–H during the hydration reactions. Decalcification of C–S–H can cause formation of zones with low C/S ratio relative to the core region resulting in the increased surface area. The N_2 adsorption technique, i.e., BET surface area technique, measures all pores and micropores present in the C–S–H. The smallest pores have the highest surface area values of BET measurements hence the higher BET surface area measurement results possibly suggest the higher fraction of smaller pores. As shown in Table 2, there was an increase in surface area for both PEG200 and HDTMA modified C–S–H samples relative to the non-modified C–S–H sample. Significantly greater increase in the surface area was observed for PEG200-CSH sample compared to the bare CSH sample (i.e., almost 58% of increase in the surface area for PEG200-CSH was observed relative to the bare CSH). BET surface area measurements suggest that both HDTMA and PEG200 contribute to increased pores or micropores within the C–S–H structure. It should be noted that the observed high BET surface area for all three samples indicate that they are fine powder-like particles or coarse cemented clusters. The synthesized C–S–H samples or polymer modified synthesized C–S–H samples used in this study are likely to be different from C–S–H gel or C–S–H(I) found in actual hydrated cement pastes or

Table 2 BET Surface area measurements of CSH and polymer modified CSH

Sample ID	Surface area (m²/g)
CSH	55.72 ± 0.51
HDTMA–CSH	59.91 ± 0.48
PEG–CSH	88.31 ± 0.52

concrete. Our synthesis method includes continuous vigorous stirring of the reaction over a period of 1 year; hence, it is not usual to find only the fine particles or majority of the particles to be in small in size contributing to high BET surface area. However, results from BET surface measurements alone do not indicate or suggest mechanistic pathways for the origin of the increased surface areas.

Figure 1 shows the XRD patterns of CSH and modified CSH samples. The collected XRD patterns of all CSH and polymer-CSH samples show the proper d-spacing for CSH structure when compared to previous studies [1, 2]. This confirms that all CSH and polymer-CSH samples are properly prepared and contains the characteristic layered structure of C–S–H(I). As shown in the Fig. 1 and the inset figure, XRD patterns of both HDTMA-CSH and PEG200-CSH samples show their d-spacing value slightly shifted to higher position of 10.312 Å relative to the one of CSH sample which occurs at 9.912 Å. This position corresponds to (002) basal plane in the layer structure of C–S–H(I) [24–26]. It is possible that the increased d_{002} spacing is likely due to the polymers included into the nanostructure of CSH. Previous studies of polymer inclusion to layered structured materials, such as clays, have suggested that expansion in the lower d-spacing values is due to the expansion of the layers caused by the polymers incorporated within the structure [5, 27–29]. Such changes in the basal spacing have been observed in similar material. Beaudoin et al. [5] have also studied synthetic C–S–H and PEG-modified C–S–H samples and observed similar extent of changes in d-spacing. With additional XRD results at lower diffraction angles, NMR experimental data, and differential thermal gravimetric analysis, they concluded that PEG treatments induced structural rearrangement of C–S–H resulting from partial intercalation or expansion.
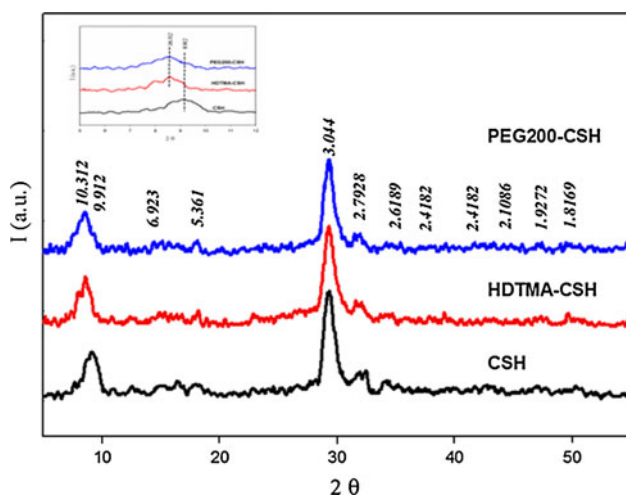
However, because of the broadening and noise in the XRD patterns for the samples and only the slight changes in the d_{002} spacing are observed, we cannot definitively conclude the inclusion of polymers into the layered structure of the CSH samples. Furthermore, it is difficult to determine whether different effects of different polymers on C–S–H structure exist or not because of the resolution of XRD patterns. Furthermore, such a small change in the basal spacing may indicate intercalation of only a small percentage of layers. For example, intercalation of one organic polymer in every seven or eight layers of the silicates may have caused such small increase in the basal spacing. More experimental results and data, such as the ones from STXM, should complement the BET and XRD results to conclude the effect of polymers on CSH nanostructures.

ATR–FTIR spectra analysis

The observed ATR–FTIR spectra of CSH and polymer-CSH samples are in a good agreement with previously reported ATR–FTIR spectra of the polymers [27, 30–32]. Figure 2 shows the ATR–FTIR spectra of the samples and the observed peaks are assigned to the different vibrational modes in accordance with generally accepted practice for the interpretation of IR spectra [33–35].

All three samples display an intense broad peak at around 1750–1650 cm^{-1} corresponding to the H–O–H bending in water molecules. The change in the position of water molecule vibration mode in this region has been the subject of a number of studies using structural, thermodynamic, spectroscopic and computational methods [36–38]. In general, it has been suggested that water molecule
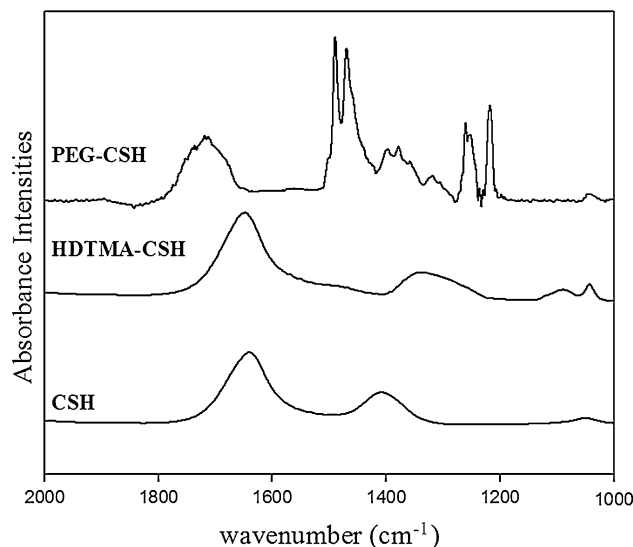

Fig. 1 XRD Patterns of CSH and polymer modified CSH. *Bold italic numbers* on the plot indicates the corresponding d-spacing to the angular measurements

Fig. 2 ATR–FTIR Spectra of CSH and polymer modified CSH

stretching band shifts to higher wavenumber upon lowering the water content strictly present in the layered structures such as clay minerals. As shown in Fig. 2, the position of this band shifted from 1636 cm^{-1} for CSH sample to 1643 cm^{-1} for HDTMA–CSH sample and 1720 cm^{-1} for PEG-CSH sample. This observation indicates that the water content within the CSH layer structure is likely to be reduced with the replacement of water molecules by hydrated HDTMA and PEG ions. Xu et al. [38] reported that water is less strongly hydrogen bonded at low water concentration within the layered clay structure and these water molecules are clustered around exchangeable cations and are polarized by the close proximity to the exchangeable cation with the oxygen in the water molecule directed toward the metal cations. Hence, the adsorption of HDTMA or PEG is likely to increase such polarization leading to a decrease in hydrogen bonding.

The infrared absorption bands for CSH at 1405 and 1052 cm^{-1} are attributed to Si–O–Si stretching vibration. The peaks at 1487 cm^{-1} for HDTMA–CSH sample are due to the methylene scissoring mode. However, the methylene scissoring mode in this sample is a broad singlet shoulder instead of a sharp doublet as previously reported for well-structured alkali tail structure. Similar broadening and reduction in the IR peaks corresponding to the methylene scissoring mode have been reported, and have been attributed to the decreased inter-chain interaction of the alkali tail molecules [39]. Others also proposed that the alkyl tails of the confined hexadecylamine are poorly packed within the silicate layers hence the confined amine does not have the same three-dimensional order as the pure amine resulting in the broadening of the band [40]. Hence, it is likely that for the adsorbed HDTMA, the amine molecules are to be confined due to its interaction with silicate chains, resulting in a competition between the amine-silicate interaction and amine–amine interaction. It has been shown that the most important factors governing the conformational behavior of the free alkanes are the nonbonded van der Waals interaction between the hydrogen atoms [40], hence at low concentration of amine, as was the case for our sample HDTMA–CSH, the interaction among amine molecules are likely to be very weak. Therefore, the broadening of the observed peak at 1467 cm^{-1} corresponding to methylene scissoring mode is most likely to be due to the amine groups interacting with silica chains in CSH.

The presence of the diagnostic bands for PEG at 1492, 1471, 1381, 1260, and 1224 cm^{-1} along with the CSH peaks at approximately 1405 and 1052 cm^{-1} as the shown in Fig. 2 indicates that PEG is adsorbed onto CSH. Similar to the HDTMA–CSH sample, the peak representing H–O–H bending in water molecules has shifted to higher wavenumbers, but the extent of peak shift was much

greater for PEG-CSH sample compared to the HDTMA–CSH sample. This observation suggests that the expansion of layers in the CSH material is likely to be greater in the presence of PEG relative to HDTMA. However, we did not observe a greater layer expansion of d_{002} plane in our XRD results for PEG-CSH sample, i.e., the d_{002} spacing was very similar for both PEG-CSH and HDTMA–CSH samples. This contradiction may arise because in XRD measurements, not only but also the outer solvent/solid interface is interrogated as bulk, whereas in ATR–FTIR measurements, only the ATR Ge crystal/solid interface is sampled. Thus, XRD evidence may be misleading if a polymer has only penetrated the outer reaches of the CSH surface or the proportion of the polymers entering the interior parts of CSH is relatively small compared to the outer surface of CSH. In contrast, the evanescent field used in ATR–FTIR measurements samples only the inner 2 μm on a sample and this means that the ATR–FTIR experiments only probes the species within the CSH-polymer film and will not be influenced by the bulk solvent in contact with the materials. Consequently, ATR–FTIR spectroscopy is considered to present a more accurate surface sensitive analysis of polymer adsorption into the bulk CSH materials, thus providing in situ information about the adsorption process. Furthermore, as shown in the STXM images (see Fig. 4) and suggested by the BET surface area measurements, the synthesized C–S–H samples and polymer modified synthesized C–S–H samples are fine powder-like particles ranging in size diameter of 2–3 μm. Hence, the polymer adsorption would be confined to a μm sized film on the external surfaces of particles that are in contact with the ATR–FTIR plate, which makes the results from ATR–FTIR measurements to be more accurate surface sensitive analysis for our samples.

Nonetheless, XRD data provides information about the ordered regions of the film whereas IR samples provide information on all the molecules within the evanescent filed regardless of the sites they occupy. Hence, we employed additional spectroscopic technique, namely STXM, to investigate the polymer-CSH interaction in further details.

STXM analysis

Figure 3 shows STXM images of CSH sample taken at C K-edge. As described in the experimental Sect. STXM (Scanning transmission X-ray microscopy) analysis, image contrast measurements, a.k.a., image mapping, identify a concentrated area of the element of interest by taking the pixel intensity before the absorption edge of the element and subtracting it from the same image taken above the absorption edge. Figure 3a is the area of clustered CSH taken at 280 eV, which is below the absorption edge of

carbon. This image is subtracted from image of the same location taken above the carbon absorption edge (300 eV) as shown in Fig. 3b. The final results, i.e., image mapping, is shown in Fig. 3c where the high concentrated carbon area is identified as bright white locations. It should be noted that image mapping only indicates and differentiates the areas of highly concentrated versus less concentrated locations. The difference in the intensities shown in Fig. 3c does not provide information on chemical speciation information of the samples. Hence, once it is confirmed that there was element of interest, then a smaller area of the image is selected and magnified to observe fine features of samples and to measure NEXAFS spectra from various locations to identify possible heterogeneity in chemical species within the samples with spatial resolution up to 25–30 nm. This is shown in Fig. 4. The smaller dotted area indicated in Fig. 3b is from which the image for Fig. 4 taken.

Figure 4a shows the STXM image and Fig. 4b shows four NEXAFS spectra taken from various locations of CSH samples. No differences among the measured four spectra were observed suggesting no heterogeneity is present with regard to carbonate penetration to CSH. The following four peaks were consistently present in our CSH samples: 284.9, 286.5, 288.4, and 290.4 eV. Using the reference spectra of previous studies [41–43], these peaks can be assigned to different carbon containing functional groups and various transition states. The observed near edge absorption bands in the range from 280 to 295 eV have been identified as the transitions to both unoccupied π^* and low lying σ^* orbitals. The small weak peak at 284.9 eV corresponds to 1 s- π^* transition with unusually low π^* states. The strong intense peak at 286.5 eV has been assigned to carbonyl functionality and peaks present around 288.4 eV have been referred to saturated carbon functional groups according to previous studies. We also observed a weak peak at 290.4 eV and this
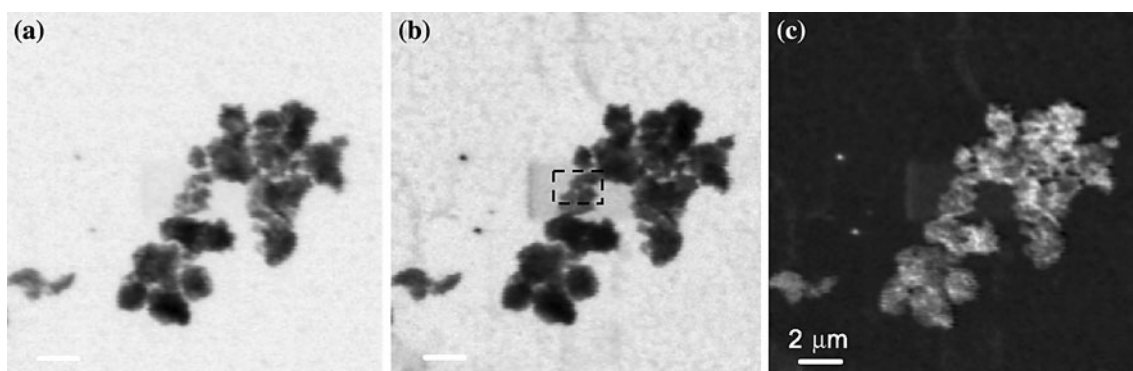

Fig. 3 STXM images of CSH taken for C K-edge at: **a** 280 eV, **b** 300 eV, and **c** image contrast (i.e., image map) of carbon edge by subtracting image (**a**) from (**b**) showing the high concentrated carbon area as bright white locations

Fig. 4 a STXM images of CSH at 300 eV. Areas enclosed in the *dotted line* and the *numbers* indicate the area where spectra of C K-edge are taken; and **b** NEXAS spectra of C K-edge taken from different locations indicated in (**a**)
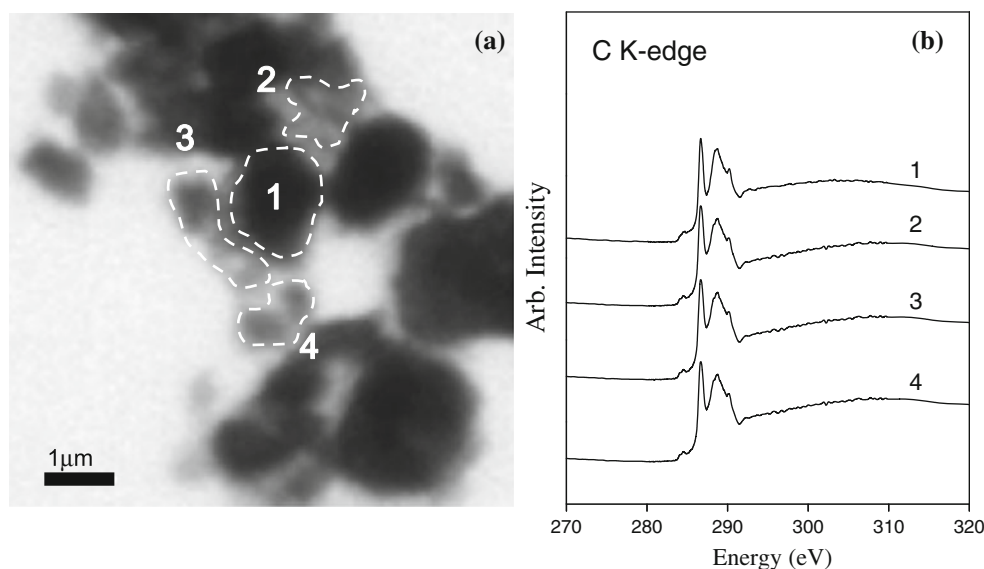
one has been identified as fingerprint for carbonate functional groups. Our obtained NEXAFS spectra agree well with the previously collected carbonate samples by Brandes et al. [44].

This observation suggests that our sample has been carbonated due to possible sorption of adventitious carbon from atmosphere. The synthesis of C–S–H materials and all the sample preparation were done under N_2 environment in the glove box, but it is impossible to avoid atmospheric CO_2 during the sample transfer from the glove box to STXM sample holder chamber. Quick loading of samples in matter of 5–10 min were practiced each time STXM measurements were performed, yet it is possible, and likely, to have immediate carbonation of the external surface area of samples. It is important to identify the location and deposition of carbon atoms due to this adventitious carbonation of the samples in detail because comparing the chemical coordination and spatial distribution of carbon atoms in samples that are exposed to carbon in different extents can provide important information on diffusion process of carbonate into the synthesized C–S–H materials.

The exact same location of our CSH sample was mapped and the corresponding NEXAFS spectra were concurrently collected at both Ca $L_{II,III}$-edge and Si K-edge as shown in Fig. 5. Similar to C K-edge NEXAFS spectra, no differences among the spectra from different locations were observed at both Ca $L_{II,III}$-edge and Si K-edge, further confirming no significant heterogeneity in the CSH sample. Ca K-edge NEXAFS spectra provide calcium coordination environment and can be used to distinguish different Ca-containing minerals that are present in C–S–H. The observed multiple peak patterns of Ca $L_{II,III}$-edge has been shown to originate from the crystal field splitting due to the first coordination sphere surrounding Ca^{2+}. The magnitudes and symmetry of the

crystal field of calcium is a good indication of arrangement of atoms around Ca^{2+}. For example, both calcite and vaterite are the polymorphs with the same chemical composition of $CaCO_3$. Calcium in these two mineral phases is coordinated by six oxygen atoms. As the results, the NEXAFS spectra peak positions and numbers are very similar for both calcite and vaterite. However, the intensity ratios for the peak occurring at 348.1 and 349.3 and at 351.4 and 352.6 eV are very different from calcite to vaterite as previous studies indicated [45, 46]. Our calcium NEXAFS spectra collected from all four locations as shown in Fig. 5a have the intensity and peak position similar to calcite, suggesting that the first coordination sphere around Ca atom in our CSH sample is similar to that of the one observed in calcite.

Si K-edge NEXAFS spectra were nosier than the ones of C K-edge or Ca $L_{II,III}$-edge as shown in Fig. 5b; nonetheless, we have observed strong spatial correlation, between silica and calcium, i.e., we observed Si wherever Ca is present, based on our results from both image contrast and NEXAFS spectral analysis. Li et al. [47] showed that Si K-edge generally shifts to higher energy in its absorption edge with increased polymerization of silicates. Our Si K-edge spectra from all four locations of CSH samples show no absorption edge shifts depending on the locations from where the spectrum was taken, suggesting that no significant differences in the silicate polymerization occurred. Si K-edge can also serve as fingerprints of local structural variations in silicate. For example, a four-oxygen coordinated Si, such as in quartz, has a Si K-edge absorption edge at around 1846.8 eV whereas six-oxygen coordinated Si, such as in stishovite, has its absorption edge at around 1858.3 eV [48, 49]. All our Si K-edge spectra have absorption edge at 1845.2 eV suggesting it is mostly four coordinated Si as in quartz.

Fig. 5 NEXAFS spectra of CSH taken at **a** Ca $L_{II,III}$-edge; and **b** Si K-edge. *Numbers* indicate the locations from where the spectra are taken as shown in Fig. 4
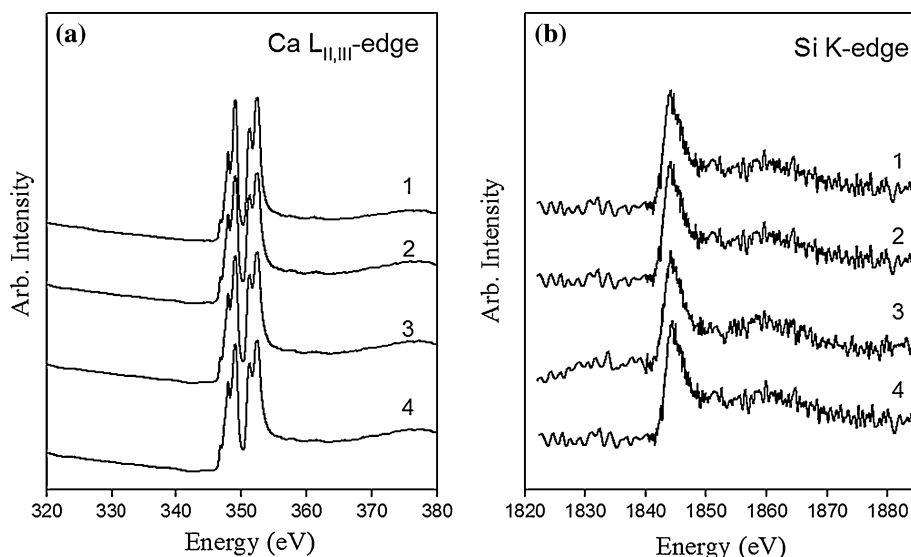
Using STXM, we have successfully observed that our synthesized CSH with Ca/Si ratio of 1.6 shows that sample is well homogenized in Ca and Si chemical compositional distribution within in the sub-micron scale.

Figure 6 shows image contrasts from three different absorption edges, i.e., Fig. 6a at C K-edge, Fig. 6b at Ca $L_{II,III}$-edge, Fig. 6c at Si K-edge, for HDTMA–CSH sample. As shown in the figure, strong spatial correlation was observed between Ca and C maps since areas with the high concentration of Ca exhibited the similar extent of high concentration of C relative to other areas. On the contrary, Si map exhibited no spatial correlation to either Ca or C. Highly concentrated Si locations (e.g., upper right round area) did not show high concentration of either Ca or C as shown in Fig. 6.

Smaller area was chosen for image stack and NEXAFS spectral analysis as shown in Fig. 7. Figure 7a shows the area from which the spectra are collected. Areas with numbers indicated in Fig. 7b were from where the NEXAFS spectra were collected for further detailed

analysis and Table 3 indicates the observed relative concentration density in the different locations at different elemental edges. As shown in the NEXAFS spectra of Fig. 7c, significant differences among the elemental spectra depending on the locations were observed. For example, C K-edge spectra from area 1 and 2 were similar to each other while they are different from the spectra collected from area 3, 4, 5, and 6 as shown in Fig. 7c. Table 3 summarizes the different peak positions observed in all six different locations. The C K-edge spectra from area 1 and 2 from HDTMA–CSH sample look very similar to the ones observed in non-polymer modified CSH sample (c.f., compare spectra in Fig. 4b and Fig. 7c). This observation suggests that HDTMA is less likely present in area 1 and 2, and that the observed carbon absorption edge is most likely due to the absorbed carbon from CO_2 in the atmosphere. However, C K-edge spectra taken from area 3 and 4 in HDTMA-CHS sample is significantly different from the spectra from area 1, 2, or CSH sample. It has several additional strong peaks as follows: the peak at 291.3 eV is
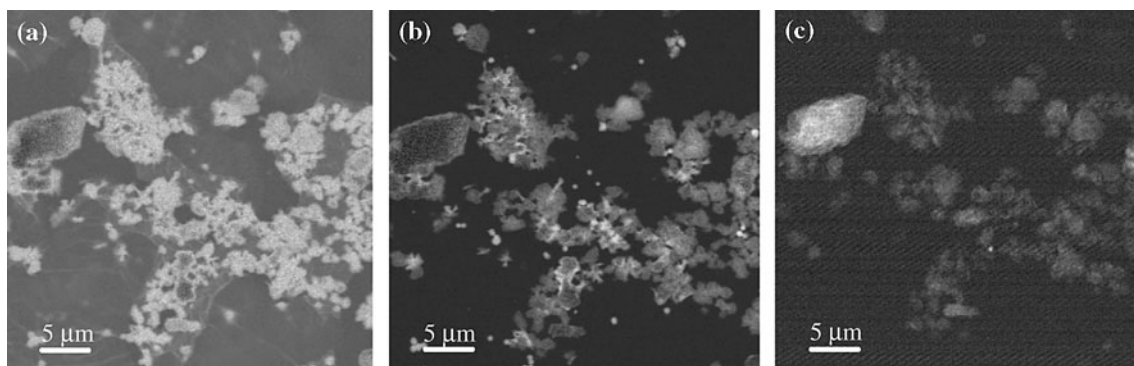

Fig. 6 STXM images contrast (i.e., image map) of HDTMA-CSH sample taken at **a** C K-edge; **b** Ca $L_{II,III}$-edge, and **c** Si K-edge. The areas with high concentrated elements are presented as *bright white* locations
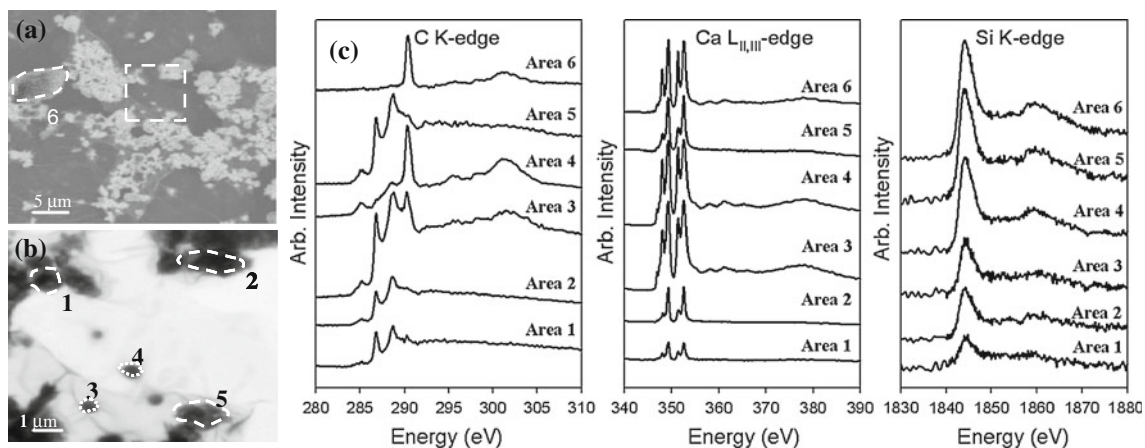

Fig. 7 STXM images and NEXAFS spectra of HDTMA-CSH sample. **a** image taken at C K-edge; **b** image of smaller area outlined in (**a**) magnifying fine structures of HDTMA–CSH sample; and **c** NEXAFS spectra at C K-edge, Ca $L_{II,III}$-edge, and Si K-edge. *Numbers* indicate the locations from where the spectra are taken as shown in (**a**) and (**b**)

Table 3 Summary of area correlation and peak positions for HDTMA–CSH samples shown in Fig. 8

Area	Relative concentrations at different elemental edges			Peak positions (eV)
	C	Ca	Si	
1	High	High	Low	C: 284.9, 286.5, 288.4, 290.4
				Ca: 357.1, 348.1, 349.3, 351.4, 352.6
				Si: 1845.2
2	High	High	Low	C: 284.9, 286.5, 288.4, 290.4
				Ca: 357.1, 348.1, 349.3, 351.4, 352.6
				Si: 1845.2
3 & 4	High	High	Very low	C: 291.3, 292.5, 295.8, 301.7
				Ca: 357.1, 348.1, 349.3, 351.4, 352.6
				Si: 1845.2, 1860 (for area 4 only)
5	High	Low	Low	C: 284.9, 286.5, 288.4, 290.4
				Ca: 357.1, 348.1, 349.3, 351.4, 352.6
				Si: 1845.2, 1860
6	Low	Low	High	C: 290.4
				Ca: 357.1, 348.1, 349.3, 351.4, 352.6
				Si: 1845.2, 1860

the well resolved 3p Rydberg peak often observed for alkane groups, the peak at 292.5 eV is the $\sigma*$ (C–C) bond that is present in HDTMA polymer, the peak at 295.8 eV is likely to be due to the $\sigma*$ (C–N) bond that is present in HDTMA polymer, and the peak at 301.7 eV is likely due to the $\pi*$ (CH$_2$) functional group in HDTMA polymer (see Table 1 for molecular structure of HDTMA). Spectrum collected from area 5 has the same number of peaks and peak positions as the spectra collected from area 1 and 2. Spectrum from area 6 is different from all the other spectra since it has a single intense peak at 290.45 eV and this one has been identified as fingerprint for carbonate functional groups. In summary, we have observed similarity in the C K-edge spectra in area 1, 2, and 5, and these spectra are different from the ones from area 3 and 4. Spectrum collected from area 6 is also singled out as different from any other spectra collected.

This correlation was also observed in Ca L$_{II,III}$-edge NEXAFS spectra as well. As noted earlier, it is important to compare the intensity ratio for the peak occurring at 348.1 and 349.3 and at 351.4 and 352.6 eV since it identifies the fine difference between the polymorphs of calcium carbonate minerals. Having the two strong doublets in Ca L$_{II,III}$-edge NEXAFS spectra of our HDTMA–CSH sample suggests that calcium in our sample is all six-coordinated by oxygen atoms. However, comparing the intensity ratio of the peaks, two different classes of calcium carbonate minerals are likely to be present in our sample. In area 1, 2, and 5, in intensity ratio for the peak occurring at 348.1 and 349.3 and at 351.4 and 352.6 eV is 1.46 $\pm$ 0.02. On the contrary, the intensity ratio of the

peaks in spectra collected from area 3 and 4 is 1.65 $\pm$ 0.05. The intensity ratio of the peaks in spectrum from area 6 is 1.52. Based on the Ca L$_{II,III}$-edge NEXAFS reference spectra, vaterite has the intensity ratios for the peak occurring at 348.1 and 349.3 and at 351.4 and 352.6 eV of 1.69 whereas calcite has the intensity ratio of 1.21. By comparing the reference spectra and our sample spectra, we conclude vaterite is more likely present in area 1, 2, and 5 whereas calcite is more likely to be present in area 3, 4, and 6. It should be noted that we did not observe any peaks associated with calcite or vaterite in our XRD measurements, yet we found an evidence of phases similar to calcite or vaterite based on our STXM measurements. This is not due to an artifact in sample preparation because STXM samples were taken out of glove chamber right before the measurements so that the exposure to ambient air should have not been greater for STXM samples. The differences in XRD and STXM data are due to the differences in the sensitivity of the two instruments. XRD takes powdered samples and observes an average of the bulk signals diffracted from the samples. Therefore, it is possible and likely, that the minor phases, especially if the phase in less than 5% of the total sample volume, is not going to be detected by the conventional laboratory-based XRD instrument. On the contrary, STXM takes measurements on a submicron level and detects signals from location by location. The carbonation reaction via exposure to the ambient air is not significant enough to generate considerable amounts of carbonated phases in our CSH samples, hence no specific peaks correlated to calcite or vaterite could have been observed by our XRD technique.

However, we able to identify the on-set of the carbonation reaction in our CSH samples using STXM.

We did not observe any significant differences in Si K-edge spectra among the sample locations. All spectra had a strong single peak at 1845.2 eV suggesting it is mostly four coordinated Si as in quartz. Small broad peak at around 1860 eV was more significant in spectra collected from area 4, 5, and 6, but it was difficult to make a definitive conclusion or spatial correlation due to the poor resolution of the spectra.

Similar experimental approach has been taken for examining the PEG–CSH sample, i.e., we took an image contrast map of all three different elements, namely Ca K-edge, Ca $L_{II,III}$-edge, and Si K-edge. Once we identified the sample locations, we took NEXAFS spectra from various different locations to probe spatial correlation among the elements and to identify chemical speciation. Figure 8 shows the summary of the experimental results with the image maps along with the NEXAFS spectra from three different absorption edges. Table 4 summarizes the spatial correlation and the NEXAFS peak positions.

Unlike the HDTMA–CSH samples, all three elements, i.e., C, Ca, and Si, showed a strong spatial correlation to each other for most of the areas as shown in the image maps in Fig. 8a–c. Smaller area was chosen to detailed analysis for compositional heterogeneity as shown in Fig. 8d. Comparing the area at different absorption edges, we found areas with high concentration of C were highly correlated to the areas with high concentration of Ca and Si (images not shown, but see Table 4 for summary). These microscopic results are supported by the spectroscopic results in which the spectra collected from high concentration of C with high concentration of Ca and Si are different from the ones of low concentration C with high concentration of Ca and Si (c.f., C K-edge spectra from area 1, 2, and 3 versus C K-edge spectra from area 4 and 5 shown in Fig. 8). C K-edge spectra collected from area 4 and 5 exhibit strong carbonate spectral features whereas the other areas exhibit strong polymer-like spectra features that are indicative of presence of PEG. This observation suggests that PEG is adsorbed to either Ca or Si. Furthermore, Ca $L_{II,III}$-edge intensity ratio for the peak occurring at 348.1 and 349.3 and at 351.4 and 352.6 eV for area 1, 2, and 3 is 1.46 ± 0.02 whereas the ratio for area 4 and 5 is 1.58 ± 0.04. Similar trend was observed for Si spectra in which area 1, 2, and 3 have absorption edges at 1845.2 eV
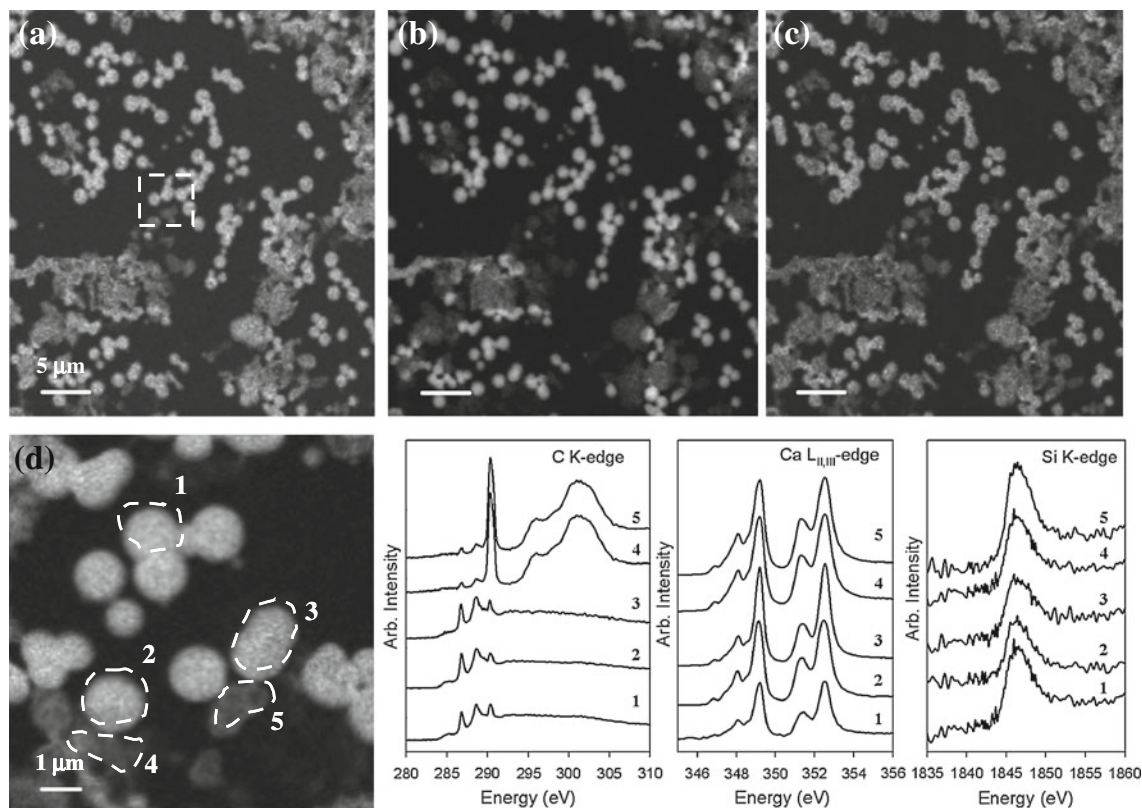

Fig. 8 STXM image maps and NEXAFS spectra of PEG-CSH sample. **a** image taken at C K-edge; **b** image taken at Ca $L_{II,III}$-edge; **c** image taken at Si K-edge; and **d** smaller area taken as shown in the dotted rectangle in (**a**) at C K-edge. NEXAFS spectra at C K-edge, Ca $L_{II,III}$-edge, and Si K-edge. *Numbers* indicate the locations from where the spectra are taken as shown in (**d**)

Table 4 Summary of area correlation and peak positions for PEG–CSH samples shown in Fig. 9

Area	Relative concentrations at different elemental edges			Peak positions (eV)
	C	Ca	Si	
1,2, & 3	High	High	High	C: 284.9, 286.5, 288.4, 290.4
				Ca: 357.1, 348.1, 349.3, 351.4, 352.6
				Si: 1845.2
4&5	Low	High	High	C: 286.5, 288.4, 290.4, 296.2, 301.5
				Ca: 357.1, 348.1, 349.3, 351.4, 352.6
				Si: 1845.2
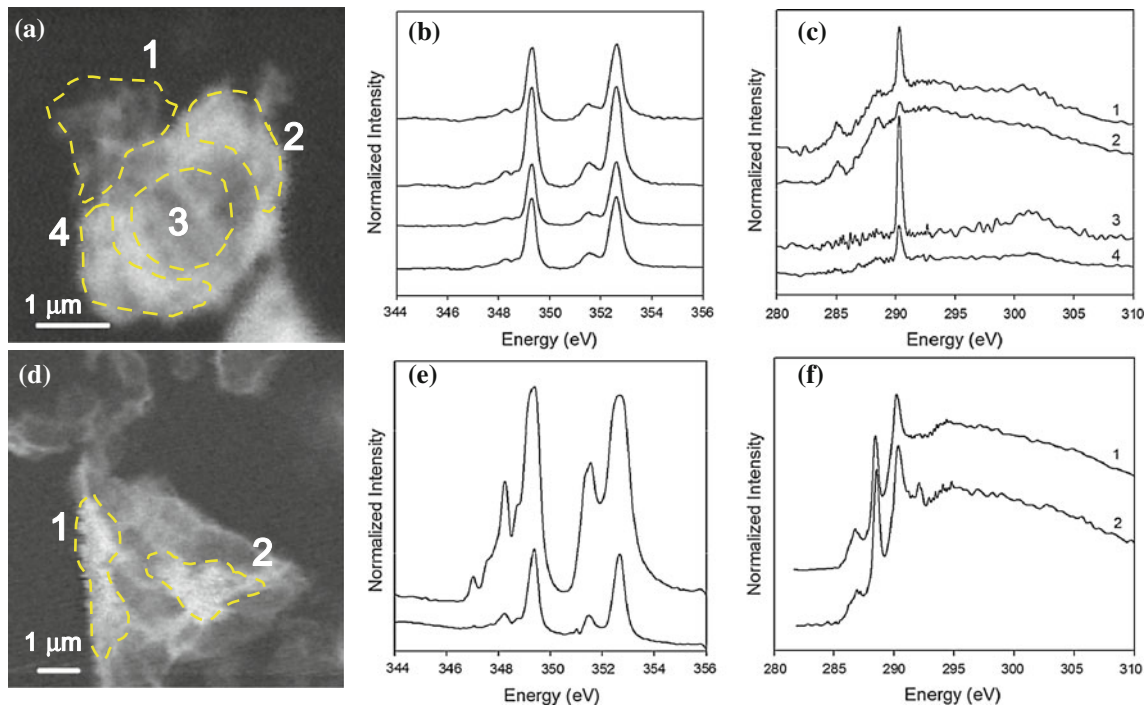
Fig. 9 STXM image maps and NEXAFS spectra of carbonated HDTMA–CSH and PEG–CSH sample. HDTMA–CSH sample: **a** STXM image taken at Ca $L_{II,III}$-edge; **b** NEXAFS spectra at C K-edge; **c** NEXAFS spectra at Ca $L_{II,III}$-edge. PEG–CSH sample: **d** STXM image taken at Ca $L_{II,III}$-edge; **e** NEXAFS spectra at C K-edge; **f** NEXAFS spectra at Ca $L_{II,III}$-edge. *Numbers* indicate the locations from where the spectra are taken as shown in (**a**) and (**d**)

whereas the spectra for area 4 and 5 have absorption edges at 1845.9 eV. These observed distinctive differences in image maps and spectral analysis among the areas we examined in PEG–CSH samples strongly suggest that PEG is strongly correlated, and most likely adsorbed, to CSH layer structures. Our results on PEG–CSH sample indicate that Ca and Si are well intermixed at a sub-micron scale with the polymer organic materials.

Figure 9 shows STXM images and C K-edge and Ca $L_{II,III}$-edge NEXAFS spectra of carbonated HDTMA–CSH and PEG–CSH samples. As shown in Ca $L_{II,III}$-edge, no calcite formed in presence of HDTMA, even though samples reacted with an intense concentration of CO_2, whereas calcite formation was suggested in presence of PEG.

Hence, it is possible that the penetrated CO_2 does not necessarily react with C–S–H to form calcite in the presence of the organic polymer HDTMA. Based on the C K-edge NEXAFS spectra, it is likely that the reacted CO_2 preserves its gaseous CO_2 configuration or incorporated into $CaCO_3$ as in the vaterite mineral phase as suggested by Ca $L_{II,III}$-edge NEXAFS spectra. Our result suggests that organic polymers interfere with CO_2 penetration into the C–S–H layer structure and hinder the precipitation reaction. However, in the absence of quantitative information on amount of CO_2 sorbed on each samples, it is difficult to conclude on the exact roles or mechanisms that the two different organic polymers play on carbonation reaction. Based on this, we can qualitatively conclude that the CO_2

reaction is likely to depend on the presence of organic polymers and on the types of organic polymers incorporated within the C–S–H structure.

Conclusions

This study has provided insight into the adsorption processes of polymers of differing charge and molecular weight into C–S–H materials. We found our synthesized CSH with C/S ratio of 1.6 was carbonated within 3–5 h of time scale. However, no heterogeneity in mineral phases with regard to Ca or Si was observed in the CSH sample due to the carbonation on such short time periods. On contrary, when polymer was adsorbed to CSH materials, we have found different Ca and Si phases. When HDTMA reacted with CSH, we found an expansion of d_{200} spacing and change in the ATR–FTIR peak representing H–O–H bending in water molecules indicating lowered water content in the layered structures. We also found an increase in the BET surface area of HDTMA–CSH sample relative to unmodified CSH sample, suggesting increased pores within the CSH materials.

The STXM data suggests that HDTMA is likely to be adsorbed to the Ca but less likely to Si, suggesting that HDTMA is likely to be adsorbed to the edges or defect sites of the layer structure of CSH. PEG–CSH sample also exhibited a d_{200} layer expansion and changes in the ATR–FTIR peak representing H–O–H bending in water molecules. However, the shift in the ATR–FTIR peak for PEG–CSH samples was greater than that of the HDTMA–CSH sample, suggesting that the exchange of water molecules with the polymer within the layer structure was greater for PEG compared to HDTMA. Furthermore, we observed a strong elemental correlation of C to both Si and Ca based on our STXM results. We observed high concentration of polymers only on the areas where significant Ca and Si present. Our spectra analysis further supports this elemental correlation. Therefore, we conclude that PEG is more readily intercalated into CSH layer structures and increase the layer spacing, which is consistent with the XRD, BET, and ATR–FTIR results. Having the considerable entropic driving for adsorption, PEG is more readily adsorbed onto the CSH compared to HDTMA. Our study further indicates CO_2 reaction strongly depends on the presence of organic polymers and the types of organic polymers incorporated within the C–S–H structure. In this study, we have shown that C–S–H layer structures are significantly modified due to the presence of the organic polymers and the chemical composition and structures of the polymers determine the extent of the C–S–H structural modifications.

References

1. Taylor HFW (1979) Cem Res Prog 9(4):89
2. Taylor HFW, Newbury DE (1985) Chatterji Cem Concr Res 15(4):741
3. Taylor HFW (1993) Adv Cem Based Mater 1(1):38
4. Cong X, James R, Kirkpatrick J, Diamond S (1993) Cem Conc Res 23:811
5. Beaudoin J, Drame H, Raki L, Alizadeh R (2009) Mater Struct 42:1003
6. Beaudoin J, Patarachao B, Raki L, Margeson J, Alizadeh R (2010) Adv Cem Res 22:15
7. Matsuyama H, Young JF (1999) Chem Mater 11(1):16
8. Morlat R, Orange G, Bomal Y, Godard P (2007) J Mater Sci 42(13):4858. doi:10.1007/s10853-006-0645-z
9. Dario M, Molera M, Allard B (2006) J Radioanal Nucl Chem 270(3):495
10. Chandra S, Flodin P (1987) Cem Concr Res 17(6):875
11. Minet J, Abramson S, Brensson B, Franceschini A, Van Dammem H, Lequex N (2006) J Mater Chem 16(14):1379
12. Merlin F, Lombois H, Joly S, Lequeux N, Halary J, VanDamme H (2002) J Mater Chem 12(11):3308
13. Wang S-D, Scrivener KL (2003) Cem Concr Res 33(5):769
14. Davydov D, Jirek M, Kopeck L Cem Concr Res (in Press)
15. Peyronnard O, Benzaazoua M, Blanc D, Moszkowicz P (2009) Cem Concr Res 39(7):600
16. Black L, Krassimir G, Gee I (2009) Cem Concr Res 38:745
17. Rees C, Provis JL, Lukey G, van Deventer J (2007) Langmuir 23:9076
18. Bell J, Sarin P, Provis J, Haggerty R, Driemeyer P, Chupas P, van Deventer J, Kriven W (2008) Chem Mater 20:4768
19. Grutzeck M, Benesi A, Fanning B (1953) J Am Ceram Soc 72(4):665
20. Tyliszczak T, Warwick AL, Kilcoyne D, Fakra S, Shuh D, Yoon T, Brown JG, Andrews S, Chembrolu V, Strachan J, Acremann Y (2004) Synchrotron Light Sour 8:1356
21. Bluhm H, Andersson K, Araki T, Benzerara K, Brown GE, Dynes JJ, Ghosal S, Gilles MK, Hansen HC, Hemminger JC, Hitchcock AP, Ketteler G, Kilcoyne ALD, Kneedler E, Lawrence JR, Leppard GG, Majzlam J, Mun BS, Myneni SCB, Nilsson A, Ogasawara H, Ogletree DF, Pecher K, Salmeron M, Shuh DK, Tonner B, Tyliszczak T, Warwick T, Yoon TH (2006) J Electron Spectrosc Relat Phenom 150(2–3):86
22. Tyliszczak T, Warwick T, Kilcoyne ALD, Fakra S, Shuh DK, Yoon TH, Brown GE Jr, Andrews S, Chembrolu V, Strachan J, Acremann Y (2004) AIP Conf Proc 705:1356
23. Hitchcock, A. P. http://unicorn.mcmaster.ca/aXis2000.html. 2000
24. Merlino S, Bonaccorsi E, Armbruster T (2001) Eur J Mineral 13:577
25. Bonaccorsiw E, Merlino S (2005) J Am Cer Soc 88(3):505

26. Merlino S, Bonaccorsi E, Armbruster T (2000) Eur J Mineral 12:411
27. He H, Ray FL, Zhu J (2004) Spectrochim Acta Part A 60A(12):2853
28. Gao F, Chen S, Hull JB (2001) J Mater Sci Lett 20(19):1807
29. Mya KY, Wang K, Chen L, Lin TT, Pallathadka PK, Pan J, He C (2008) Macromol Chem Phys 209(6):643
30. Amelina EA, Kuksenova LI, Parfenova AM, Rybakova LM, Bessonov AI, Shchukin ED (1997) Colloid J (Transl Kolloidn Zh) 59(6):673
31. Mert O, Doganci E, Erbil HY, Demir AS (2008) Langmuir 24(3):749
32. Billingham J, Breen C, Yarwood J (1997) Vib Spectrosc 14(1):19
33. Kuptsov AH, Zhizhin GN (1998) (Eds) In: Handbook of Fourier transform raman and infrared spectra of polymers
34. Nakamoto K (ed) (2009) Infrared and Raman spectra of inorganic and coordination compounds, part A: theory and applications in inorganic chemistry, 6th edn
35. Nakamoto K (ed) (2009) Infrared and Raman spectra of inorganic and coordination compounds, part B: applications in coordination, organometallic, and bioinorganic chemistry, 6th edn
36. Cases JM, Bérend I, François M, Uriot JP, Michot LJ, Thomas F (1997) Clays Clay Minerals 45:8
37. Yan L, Low P, Roth C (1996) Clays Clay Minerals 44:744
38. Xu W, Johnston C, Parker P, Agnew S (2000) Clays Clay Mineral 48:120
39. Venkataraman NV, Vasudevan S (2001) J Phys Chem B 105(9):1805
40. Li Y, Ishida H (2003) Langmuir 19(6):2479
41. Francis JT, Hitchcock AP (2002) J Phys Chem 96(16):6598
42. Myneni SCB (2002) Rev Mineral Geochem 49:485
43. Hitchcock AP, Urquhart SG, Rightor EG (2002) J Phys Chem 96(22):8736
44. Brandes JA, Lee C, Wakeham S, Peterson M, Jacobsen C, Wirick S, Cody G (2004) Mar Chem 92(1–4):107
45. Ha J, Chae S, Chou KW, Tyliszczak T, Monteiro PJM (2010) Transp Res Rec 2142:83
46. Obst M, Dynes JJ, Lawrence JR, Swerhone GDW, Benzerara K, Karunakaran C, Kaznatcheev K, Tyliszczak T, Hitchcock AP (2009) Geochim Cosmochim Acta 73(14):4180
47. Li D, Bancroft GM, Fleet ME, Feng XH (1995) Phys Chem Mineral 22(2):115
48. Mo S-D, Ching WY (2001) Appl Phys Lett 78(24):3809
49. Flank AM, Trcera N, Brunet F, Itie JP, Irifune T, Lagarde P (2009) Experimental evidece of six-fold ocygen coordination for phosphorous and XANES calculations. In: 14th International conference on X-ray absorption fine strucutres, vol 190, p 012174